CONTRAST MEDIA & MOLECULAR IMAGING

Received: 4 December 2011, Revised: 14 June 2012, Accepted: 18 June 2012, Published online in Wiley Online Library:

(wileyonlinelibrary.com) DOI: 10.1002/cmmi.1485

Optical imaging of progenitor cell homing to patient-derived tumors

Isabel G. Newton[a]*, Warren C. Plaisted[a], Steven Messina-Graham[a], Annelie E. Abrahamsson Schairer[a], Alice Y. Shih[a], Evan Y. Snyder[a,b], Catriona H. M. Jamieson[a] and Robert F. Mattrey[a]

Capitalizing on cellular homing to cancer is a promising strategy for targeting malignant cells for diagnostic, monitoring and therapeutic purposes. Murine C17.2 neural progenitor cells (NPC) demonstrate a tropism for cell line-derived tumors, but their affinity for patient-derived tumors is unknown. We tested the hypothesis that NPC accumulate in patient-derived tumors at levels detectable by optical imaging. Mice bearing solid tumors after transplantation with patient-derived leukemia cells and untransplanted controls received 10^6 fluorescent DiR-labeled NPC daily for 1–4 days, were imaged, then sacrificed. Tissues were analyzed by immunofluorescence and flow cytometry to detect tumor cell engraftment (CD45) and NPC (FITC-β galactosidase or DiR). Tumors consisted primarily of CD45-positive cells and demonstrated mild fluorescence, corresponding to frequent clusters of FITC-β gal-positive cells. Both transplanted and control mice demonstrated the highest fluorescent signal in the spleens and other tissues of the reticuloendothelial activating system. However, only rare FITC-β gal-positive cells were detected in the mildly engrafted transplanted spleens and none in the control spleens, suggesting that their high DiR signal reflects the sequestration of DiR-positive debris. The mildly engrafted transplanted kidneys demonstrated low fluorescent signal and rare FITC-β gal-positive cells whereas control kidneys were negative. Results indicate that NPC accumulate in tissues containing patient-derived tumor cells in a manner that is detectable by *ex vivo* optical imaging and proportional to the level of tumor engraftment, suggesting a capacity to home to micrometastatic disease. As such, NPC could have significant clinical applications for the targeted diagnosis and treatment of cancer. Copyright © 2012 John Wiley & Sons, Ltd.

Keywords: cellular imaging; homing; fluorescent probes; C17.2; chronic myeloid leukemia; neural progenitor cells; humanized cancer model; immunofluorescence; FACS

1. INTRODUCTION

A significant challenge in cancer and imaging research is the development of methods to target malignant cells for diagnostic, monitoring and therapeutic purposes. Strategies that aim to target cancer cells directly require knowledge of a cancer's specific cellular and molecular identity, which differs among cancers, among patients with the same diagnosis and even within any given patient (1). This approach is challenging and costly and leads to the need for highly personalized medicine.

A promising alternative strategy is to target cancer cells indirectly by exploiting the natural propensity of some progenitor and stem cells to home to tumor sites (2–9). The tumor-seeking properties of mesenchymal stem cells, C17.2 murine neural progenitor cells (NPC; Table 1) and human NPC have been studied extensively; these cells can be labeled with a contrast agent and imaged to reveal sites of cancer using a variety of modalities (5,7,10–14) or used to deliver therapeutic molecules or genes (10,15–22). Mesenchymal stem cells demonstrate robust homing to tumor sites and are readily available from adipose tissue and bone marrow (5,6); however, evidence that mesenchymal stem cells support tumor growth and spread (23,24) raises major concerns regarding their clinical applications. NPC have not been shown to demonstrate these properties and thus may represent a safer alternative.

Studies have shown that C17.2 NPC administered by tail vein injection ($2–3 \times 10^6$ cells) accumulate preferentially in cutaneous melanoma masses and intracranial glioblastoma tumors as early as 30 min post-injection and persist at 4 days (4) and 6 days post-injection (2). Similarly, C17.2 NPC concentrate in Lewis lung carcinoma tumors at 24 and 48 h after intravenous doses of 5×10^5 cells, visible by bioluminescence imaging and gamma imaging with Indium-111 (3). Not only do C17.2 NPC remain viable at these time points and retain their capacity to express prodrug-activating enzymes and prodrugs, but they also target small clusters of tumor cells and even individual tumor cells that have migrated away from the original tumor mass, suggesting a tropism for metastatic cells (2). Until now, studies of NPC homing to cancer have concentrated on tumors derived from cell lines

* *Correspondence to: I. G. Newton, UCSD Medical Center, Radiology Department, 200 West Arbor Drive, San Diego, CA 92103–8756, USA. E-mail: inewton@ucsd.edu*

a *I. G. Newton, W. C. Plaisted, S. Messina-Graham, A. E. Abrahamsson Schairer, A. Y. Shih, E. Y. Snyder, C. H. M. Jamieson, R. F. Mattrey*
University of California, San Diego, CA 92103-8756, USA

b *E. Y. Snyder*
Sanford-Burnham Medical Research Institute, 10901 North Torrey Pines Road, La Jolla, CA 92037, USA

Table 1. List of Common Abbreviations

FITC-β gal	FITC-conjugated β galactosidase antibody
C17.2	Murine cerebellum-derived neural progenitor cells
CML	Patient-derived blast crisis chronic myeloid leukemia
DiR	Lipophilic near infrared fluorescent dye, 1, 1′-dioctadecyl-3,3,3′,3′-tetramethylindotricarbocyanine iodide
DiR-C17.2	DiR-labeled C17.2 cells
FACS	Fluorescence-activated flow cytometric analysis and cell sorting
IF	Immunofluorescence histologic analysis
NPC	Neural progenitor cells
C/0	Control untransplanted mouse, no C17.2 cells
CML/0	CML-transplanted mouse, no C17.2 cells
C/C17.2	Control untransplanted mouse injected with DiR-C17.2 cells i.v.
CML/C17.2	CML-transplanted mouse injected with DiR-C17.2 cells i.v.

whereas patient-derived tumors are more likely to reflect the heterogeneity and metastatic properties that cancer exhibits clinically (25,26).

Tumors grown from cancer cells harvested from patients differ from those grown from immortalized cancer cell lines in many important ways. Patient cancer cells represent a heterogeneous population consisting of cancer stem cells and differentiated cancer cell types that give rise to solid tumors that interact with the environment to recruit stromal cells and blood vessels to support their growth (1,27,28). Cancer cell lines exhibit far less heterogeneity by virtue of being an immortalized clonal cell line. Moreover, most patient-derived cancer cells have specialized niche requirements and require transplantation into nutrient-rich environments such as the liver (28), bone marrow (29) or kidney, and will not survive subcutaneous or intravenous injection, as do cells from cancer cell lines (18). This niche requirement suggests a more complex interaction between patient-derived cancer cells and local and systemic signals, including chemokines, growth factors and components of the immune system (24). Also, just like the tumors from which they were harvested, patient-derived tumors grow over a matter of months whereas cell line-derived tumors can reach the same size in a matter of weeks (28). Finally, patient-derived tumors demonstrate a complex metastatic profile, with solid tumors and tumor cell engraftment detectable at distant sites from transplantation, in a pattern of spread that mirrors that observed in the donor patient (25,28). An excellent model for studying the complex interactions between tumor-tropic NPC and patient-derived tumors is the murine xenograft of patient-derived chronic myeloid leukemia (CML).

CML was the first cancer demonstrated to arise at the level of the hematopoietic stem cell, owing to a genetic translocation producing the Philadelphia chromosome which encodes the constitutively activated tyrosine kinase, P210BCR-ABL (28,30–33). This discovery led to the development of the first molecularly targeted anticancer drug, the BCR-ABL tyrosine kinase inhibitor imatinib (31). Although the incidence of CML is just under 5000 cases per year in the USA, its prevalence rises annually owing to successes in imatinib treatment that have resulted in a dramatic drop in mortality to approximately 2% (34). In the absence of imatinib treatment and sometimes in spite of it, because of resistance, some patients will go on to progress to blast crisis CML, a more aggressive phase of the disease with a course similar to acute leukemia, with rapid progression and decreased survival. Studies in our laboratory of patient-derived CML cells in a murine CML xenograft model have revealed that this progression of CML from chronic phase to blast crisis involves the activation of the Wnt/β-catenin self-renewal pathway in a population of granulocyte-macrophage progenitor cells (28,35). Research continues to focus on understanding the cellular and molecular pathogenesis of CML. Thus, CML represents an excellent model to investigate the tropism of NPCs for the diverse population of patient-derived cancer cells that includes cancer stem cells.

The development of new anticancer theragnostic technologies with the greatest potential for application in humans requires the establishment of a reliable animal model of cellular homing to patient-derived tumors using a sensitive imaging modality that can be performed easily and repeatedly. To this end, we used fluorescence imaging with the near-infrared lipophilic dye 1,1′-dioctadecyl-3,3,3′,3′-tetramethylindotricarbocyanine iodide (DiR) to test the hypothesis that C17.2 NPC home to patient-derived CML tumors at levels detectable by optical imaging. DiR is well-suited for *in vivo* cellular tracing owing to its relatively good tissue penetration and resistance to photobleaching. The distribution of fluorescent signal after intravenous injection of DiR-labeled cells reflects a variety of factors, including cell trapping in the pulmonary capillary bed, sequestration of cells and debris by the phagocytic mononuclear cells (which are rich in the liver, spleen, marrow and lung), and active cellular homing into the parenchyma of target tissues. As such, fluorescence-activated cell sorting (FACS) and immunofluorescence histologic analysis (IF) were used to assess the proportion and distribution of C17.2 cells in various tissues in relation to human tumor cell engraftment. The results show that C17.2 NPC home to tissues engrafted with CD45+ CML cells in a manner proportionate to the level of cancer cell engraftment and that this homing is detectable by *ex vivo* optical imaging. These data suggest that C17.2 NPC not only target solid tumors but also accumulate in tissues containing individual cancer cells, suggesting a tropism for micrometastatic disease. Thus, cellular homing to patient-derived solid tumors and micrometastases could be adapted clinically for the diagnosis of cancer and the targeted delivery of treatment.

2. RESULTS

2.1. Optical fluorescence imaging

Using C/0 or CML/0 mice as negative controls, C/C17.2 and CML/C17.2 mice were imaged optically approximately 3 h after daily DiR-C17.2 injections for up to 4 days, for a maximal possible dose of 4.5×10^6 cells for the 96 h mice, with subsets of mice sacrificed at each of the 24, 48, 72 and 96 h time points (see Experimental section for details). These time points were selected based on the literature, which indicates that NPC concentrate in tumors as early as 30 min after injection and remain viable within tumors at 4 and 6 days (2–4). Cells were dosed daily to increase the total DiR-C17.2 cell dose while avoiding increased mortality observed after injections of greater than 1.5×10^6 cells. Daily imaging was performed both to confirm intravenous delivery of the cells and to evaluate whether NPC homing to patient-derived CML

tumors follows a similar time course to cell-line derived tumors; however, it was not a primary end point of this study to investigate the temporal characteristics of NPC homing.

Within the first hour after injection of DiR-C17.2 cells, fluorescent signal appeared in the thorax, corresponding to the lungs on postmortem imaging (data not shown). By 24 h post-injection, the signal appeared in the upper abdomen, corresponding to the liver and spleen on postmortem imaging, and in the bone marrow. This pattern of fluorescent signal persisted without significant change through the 48, 72 and 96 h time points examined. Mice shown in Fig. 1 are from the 72 and 96 h time points and are representative of the pattern of fluorescence seen

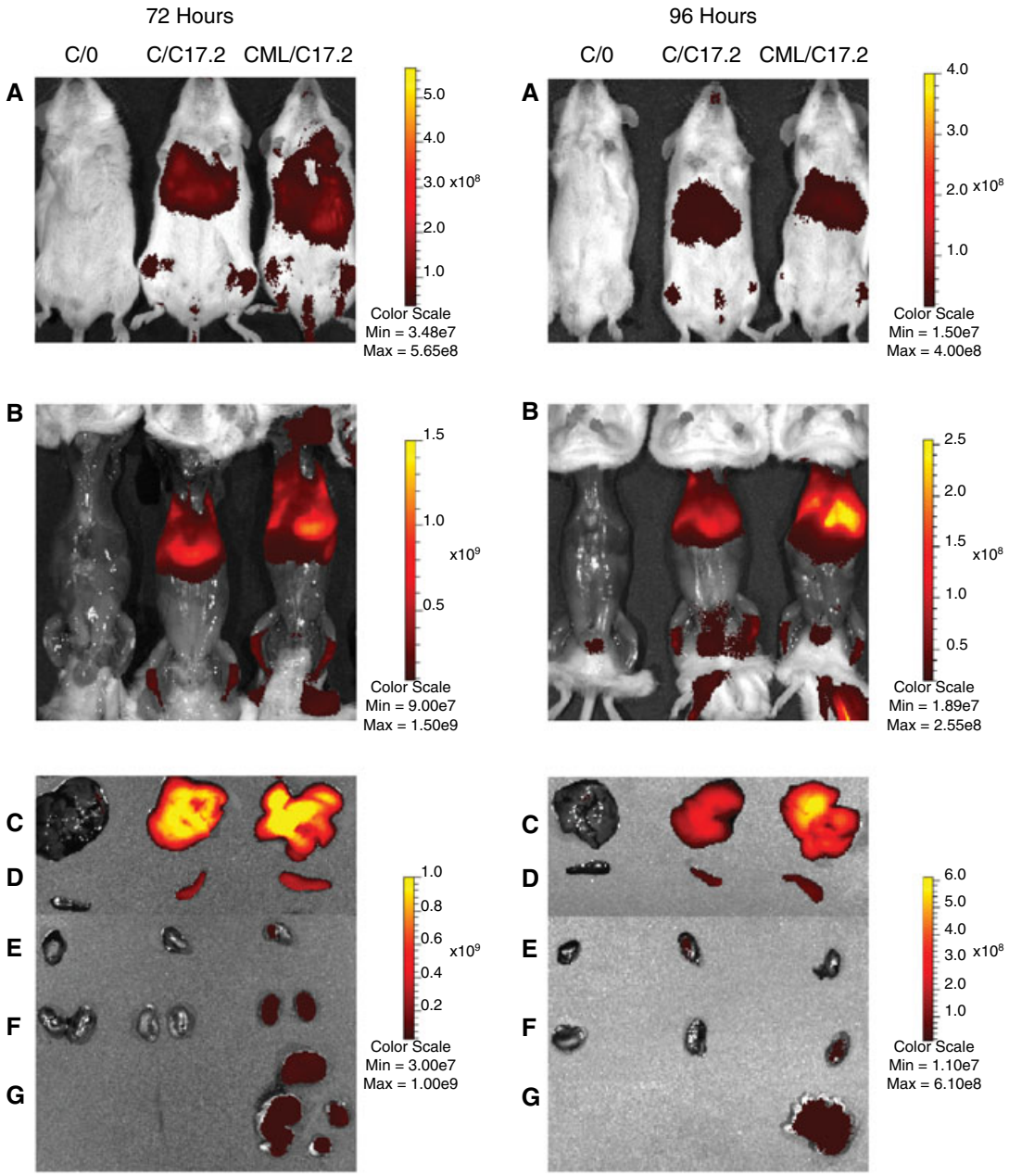

Figure 1. Fluorescence imaging of mice at 72 h (left) and 96 h (right) after the first of daily intravenous injections of DiR-C17.2 cells. The total dose administered was 4×10^6 cells for the 72 h mice and 4.5×10^6 cells for the 96 h mice. Control (C/0) mice and tissues are displayed in the first column of each time point, C/C17.2 mice and tissues in the second column and CML/C17.2 mice and tissues in the third column. Mice shown are representative not only of their respective time points but also of the pattern of fluorescence seen in C/C17.2 and CML/C17.2 mice by 24 and 48 h post-injection (data not shown). (A) On *in vivo* imaging, there is robust fluorescent signal within the thorax and upper abdomen of both the C/C17.2 mouse (second column of each time point) and CML/C17.2 mice (third column of each time point) as compared with C/0 controls (first column of each time point). Fluorescent signal in the lower extremities is detectable in both C/C17.2 and CML/C17.2 mice. (B) Imaging of the same mice with the skin deflected to reveal DiR signal in the lungs, liver, spleen and marrow in both the C/17.2 and CML/C17.2 mice. The bottom panels demonstrate *ex vivo* imaging of the organs of these mice using a 5 s exposure, confirming high fluorescent signal within the C/C17.2 and CML/C17.2 liver (C) and spleen (D) as compared with the negative C/0 tissues. *Ex vivo* imaging of the heart (E) and kidneys (F) of these mice using a 10 s exposure reveals a mild DiR signal in these tissues of both the C/C17.2 and CML/C17.2 mice and mild signal in the tumors (G) of the CML/C17.2 mice. The tissues of C/0 mice are negative.

in C/C17.2 and CML/C17.2 mice by 24 and 48 h post-injection, as well; for that reason, the 24 and 48 h time points are not shown separately. Postmortem *in situ* imaging (Fig. 1B) and *ex vivo* organ imaging confirmed high fluorescent signal within the C/C17.2 and CML/C17.2 liver (C) and spleen (D) and mild signal in the heart (E), kidneys (F) and tumor (G) of these mice as compared with the negative C/0 or CML/0 tissues. Fluorescence from superficial tumors was detectable *in vivo* but detection of signal from deeper tumors was improved by reflection of the overlying soft tissues and fur or by *ex vivo* imaging.

Average radiances (p/s/cm^2/sr) of tissues of DiR-C17.2-injected mice compared with controls that did not receive DiR-C17.2 injections are demonstrated in Fig. 2. DiR-C17.2-injected mice include C/C17.2 ($N = 5$ per tissue) and CML/C17.2 ($N = 19$ livers, 13 spleens, 12 marrow, 21 tumors, 17 kidneys and 11 hearts). Controls that did not receive DiR-C17.2 injections include C/0 and CML/0 and are collectively referred to as 'No DiR-C17.2' ($N = 2$ for all tissues except spleen and tumor, $N = 1$). The variations in N reflect the fact that not all tissues emitted a measurable fluorescent signal and, rather than arbitrarily assign them a zero value, they were not included in the statistical analysis. The average radiance of all No DiR-C17.2 livers, spleens, marrow, tumors and kidneys that emitted measurable fluorescence was calculated ($7.6 \times 10^6 \pm 1.3 \times 10^6$ p/s/cm^2/sr, $N = 10$) and referred to as the 'All Tissues' control in Fig. 2.

All C/C17.2 and CML/C17.2 tissues, including CML/C17.2 tumors, emitted a fluorescent signal that was significantly greater than background levels of the All Tissues control (Fig. 2). All but one of the tumors imaged *ex vivo* demonstrated positive fluorescence (defined as $\geq 9 \times 10^6$ p/s/cm^2/sr), with an average tumor fluorescence of $2.6 \times 10^7 \pm 2.4 \times 10^7$ p/s/cm^2/sr, whereas the tumors from CML/0 mice were negative. There are no statistically significant differences between the fluorescent signals of the C/C17.2 and CML/C17.2 tissues for the liver, spleen, marrow, kidneys or heart. The highest fluorescent signal was detected in the lungs (C/C17.2: 1.29×10^9 p/s/cm^2/sr, CML/C17.2: 7.8×10^8 p/s/cm^2/sr, data not graphed), liver (C/C17.2: 3.9×10^8 p/s/cm^2/sr, CML/C17.2: 2.4×10^8 p/s/cm^2/sr) and spleen (C/C17.2: 1.7×10^8 p/s/cm^2/sr, CML/C17.2: 1.5×10^8 p/s/cm^2/sr) with lower levels in the bone marrow (C/C17.2: 1.2×10^7 p/s/cm^2/sr, CML/C17.2: 2.3×10^7 p/s/cm^2/sr), kidneys (C/C17.2: 2.4×10^7 p/s/cm^2/sr, CML/C17.2: 2.0×10^7 p/s/cm^2/sr) and hearts (C/C17.2: 1.7×10^7 p/s/cm^2/sr, CML/C17.2: 2.5×10^7 p/s/cm^2/sr).

In summary, both C/C17.2 and CML/C17.2 mice demonstrated similar patterns of fluorescent signal after i.v. injection of DiR-C17.2 cells, with signal appearing first in the lungs immediately post-injection but then in the livers and spleens, marrow, kidneys, hearts and, when present, tumors by 24 h post-initial injection in a pattern that persisted at 48, 72 and 96 h. Because the pattern of fluorescent signal did not change after 24 h and there were no significant differences among time points for any of the analyses performed, the data from these time points were pooled for the subsequent analyses.

2.2. FACS

2.2.1. CD45-positive human cancer cell engraftment

Human cancer cell engraftment, as indicated by the average percentage of live cells expressing the human cell marker CD45, was analyzed by FACS in tissues of the untransplanted Control (both C/0 and C/C17.2; $N = 6$) vs CML-transplanted mice (both CML/0 and CML/C17.2; $N = 24$ for all tissues except spleen, $N = 15$; Fig. 3). The average nonspecific background CD45 staining in all Control livers, spleens, marrow and kidneys was calculated for comparison ($4.0 \pm 5.9\%$, $N = 19$) and referred to as the 'All Tissues' control in Fig. 3.

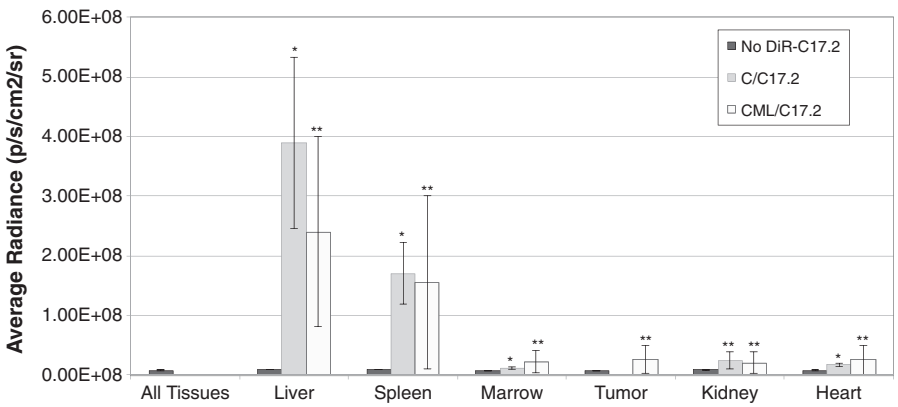

Figure 2. Average radiances (p/s/cm^2/sr) of tissues of DiR-C17.2-injected mice vs controls that did not receive DiR-C17.2 injections. DiR-C17.2-injected mice include C/C17.2 (medium gray, $N = 5$ per tissue) and CML/C17.2 (light gray, $N = 19$ livers, 13 spleens, 12 marrow, 21 tumors, 17 kidneys and 11 hearts). Controls that did not receive DiR-C17.2 injections include C/0 and CML/0 and are collectively referred to as 'No DiR-C17.2' (dark gray; $N = 2$ for all tissues except spleen and tumor, $N = 1$). The variations in N reflect the fact that not all tissues emitted measurable fluorescent signal; rather than assign these tissues a zero value, they were not included in the statistical analysis. 'All Tissues' represents the average radiance of all No DiR-C17.2 livers, spleens, marrow, tumors and kidneys that emitted measurable background fluorescence ($7.6 \times 10^6 \pm 1.3 \times 10^6$ p/s/cm^2/sr, $N = 10$). Statistical significance ($p < 0.05$) is denoted with two asterisks when compared with All Tissues and by a single asterisk when compared with both the No DiR-C17.2 control for the same tissue and to the All Tissues control. All C/C17.2 and CML/C17.2 tissues emitted fluorescent signal that was significantly greater than background levels of the All Tissues control. There are no statistically significant differences between the fluorescent signals of the C/C17.2 and CML/C17.2 tissues for any tissue measured. The highest fluorescent signal was detected in the lungs (C/C17.2, 1.29×10^9 p/s/cm^2/sr; CML/C17.2, 7.8×10^8 p/s/cm^2/sr, data not graphed), liver (C/C17.2, 3.9×10^8 p/s/cm^2/sr; CML/C17.2, 2.4×10^8 p/s/cm^2/sr) and spleen (C/C17.2, 1.7×10^8 p/s/cm^2/sr; CML/C17.2, 1.5×10^8 p/s/cm^2/sr) with lower levels in the bone marrow (C/C17.2, 1.2×10^7 p/s/cm^2/sr; CML/C17.2, 2.3×10^7 p/s/cm^2/sr), tumors (CML/C17.2, 2.6×10^7 p/s/cm^2/sr), kidneys (C/C17.2, 2.4×10^7 p/s/cm^2/sr; CML/C17.2, 2.0×10^7 p/s/cm^2/sr) and hearts (C/C17.2, 1.7×10^7 p/s/cm^2/sr; CML/C17.2, 2.5×10^7 p/s/cm^2/sr).

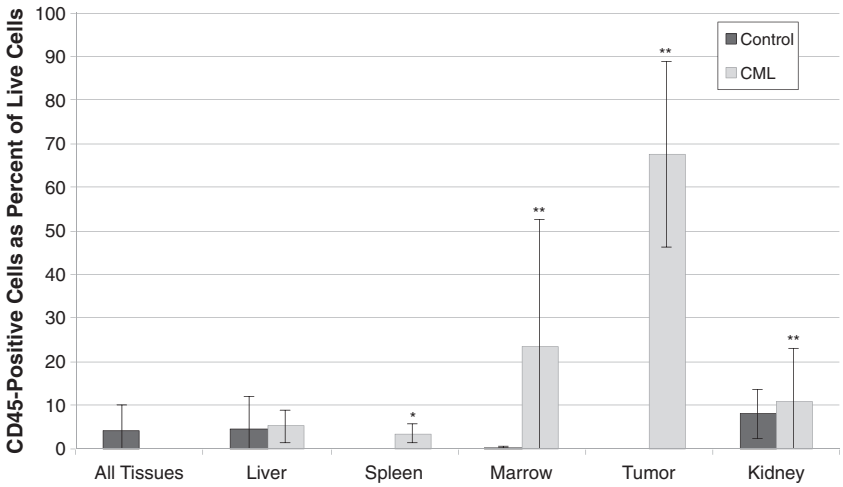

Figure 3. Human cancer cell engraftment in tissues of Control (both C/0 and C/C17.2; dark gray, $N = 6$) vs CML-transplanted mice (both CML/0 and CML/C17.2; light gray, $N = 24$ for all tissues except spleen, $N = 15$), as indicated by the average percentage of live cells expressing the human cell marker CD45. 'All Tissues' represents the average of the percent engraftment of all Control livers, spleens, marrow and kidneys ($4.0 \pm 5.9\%$, $N = 19$). Statistical significance ($p < 0.05$) is denoted with two asterisks when compared with the All Tissues control and with a single asterisk when compared with the Control spleens. CML marrow, tumors and kidneys demonstrated significantly higher levels of engraftment than the untransplanted All Tissues control and CML splenic engraftment ($3.5 \pm 2.2\%$) was significantly greater than Control spleens (0%). Tumors demonstrated the highest engraftment levels, with live CD45-positive cells comprising $67.6 \pm 21.4\%$ of cells analyzed. The wide variance in the CML bone marrow engraftment ($23.4 \pm 29.1\%$) reflects variations in patient cancer profiles: engraftment was $53.3 \pm 25.6\%$ in one patient sample vs 0.66% in controls, but $1.7 \pm 0.6\%$ in another patient sample, which was not significantly different from controls. Wide patient cancer-specific variation was also observed in the renal engraftment (the average of $10.7 \pm 12.5\%$ vs 8.0% in controls includes data from one experiment where the average was $0.26 \pm 0.31\%$, vs 0.08% in control kidneys). There was no statistically significant difference between liver engraftment ($5.2 \pm 3.8\%$) and background CD45 staining in control livers (4.4%) or the All Tissues control.

CML tumors, marrow and kidneys demonstrated engraftment levels that were significantly higher than background levels in the untransplanted All Tissues control. CML engraftment in spleens ($3.5 \pm 2.2\%$) was significantly greater when compared with Control spleens (0%). Tumors demonstrated the highest engraftment levels, with live CD45-positive cells comprising $67.6 \pm 21.4\%$ of cells analyzed. CML bone marrow engraftment differed by patient sample, with live CD45-positive cells representing $53.3 \pm 25.6\%$ of cells analyzed in one patient sample (vs 0.66% in controls) but only $1.7 \pm 0.6\%$ in another patient sample (vs $2.3 \pm 1.5\%$ in controls). This difference in levels of bone marrow engraftment among patient samples has been observed across numerous experiments in our laboratory and is believed to reflect the inherent heterogeneity of CML among patients. Wide variations in levels of renal engraftment among tumors derived from different patient samples was also observed; the average renal engraftment level of 10.7 ± 12.5 vs 8.0% in controls includes data from one experiment where the average was 0.26 ± 0.31 vs 0.08% in control kidneys. There was no statistically significant difference between liver engraftment ($5.2 \pm 3.8\%$) and background CD45 staining in control livers (4.4%) or the All Tissues control.

2.2.2. *DiR-positive cells*

The proportion of DiR-positive cells in the tissues of control and DiR-C17.2 cell-injected mice was evaluated by FACS (Fig. 4). DiR-C17.2-injected mice include C/C17.2 ($N = 4$ per tissue except for spleen, $N = 0$ owing to processing error) and CML/C17.2 ($N = 22$ per tissue except for spleen, $N = 15$). Controls that did not receive DiR-C17.2 injections include C/0 and CML/0 and are collectively referred to as 'No DiR-C17.2' ($N = 4$ for all tissues except spleen and tumor, $N = 2$). The average percentage of DiR-positive cells in all No DiR-C17.2 livers, spleens, marrow, tumors and kidneys ($0.35 \pm 0.22\%$, $N = 16$) comprises the 'All Tissues' control in Fig. 4.

Tumors showed a significantly higher proportion of DiR-positive cells as compared with the All Tissues control. Both C/C17.2 and CML/C17.2 livers and marrow and CML/C17.2 spleens and kidneys demonstrated higher proportions of DiR-positive cells than their respective tissue-matched controls and the All Tissues control (Fig. 4). There was no significant difference in the percentage of DiR-positive cells in the C/C17.2 vs CML/C17.2 livers, spleens, marrow or kidneys. The average percentage of DiR positive cells in tissues $\pm$ SD was as follows: livers (C/C17.2: $1.81 \pm 0.44\%$, CML/C17.2: $7.76 \pm 5.79\%$), marrow (C/C17.2: $1.50 \pm 0.66\%$, CML/C17.2: $2.13 \pm 1.37\%$), spleens (C/C17.2: $1.81 \pm 0.44\%$, CML/C17.2: $7.76 \pm 5.79\%$), tumors (CML/C17.2: $0.74 \pm 0.61\%$) and kidneys (C/C17.2: $0.56 \pm 0.04\%$, CML/C17.2: $1.00 \pm 0.48\%$). Interestingly, there was a higher proportion of DiR-positive cells in the bone marrow that contained 53% engraftment ($2.8 \pm 1.7\%$) than in the marrow with 0.19% engraftment ($1.7 \pm 0.6\%$).

2.3. IF

IF was performed on tissues using an anti-β-galactosidase antibody conjugated to FITC to evaluate for C17.2 cells and anti-CD45 antibodies conjugated to Alexa 488 or Alexa 647 to evaluate for human cancer cell engraftment (see Experimental for details). Analysis was performed on CML/C17.2 tumors as well as the spleens and kidneys of C/0, C/C17.2 and CML/C17.2 mice. These experiments demonstrated that CML tumors consist primarily of CD45-positive human cells (≥400 cells per high powered field, or ≥83%; Fig. 5) whereas CD45-positive cells were rare in CML spleens (0–2 per high-powered field, or ≤0.2%; Fig. 6) and in CML kidneys (0–1 per high-powered field, or ≤0.5%; Fig. 7).

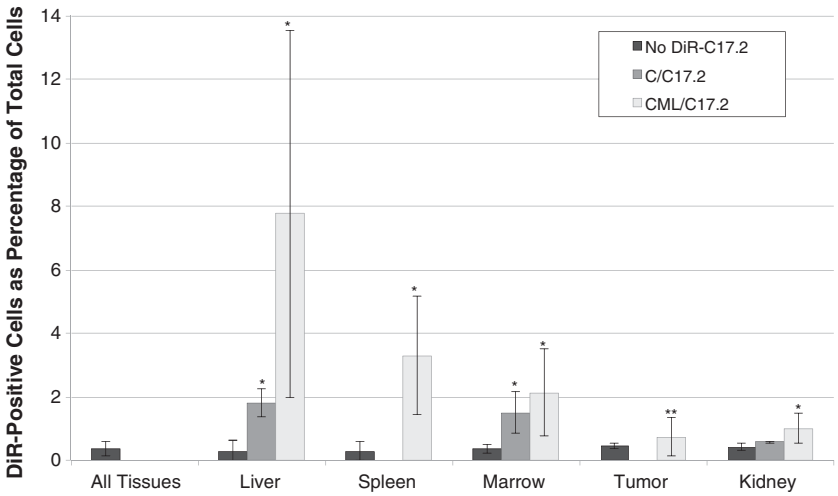

Figure 4. Average percentage of DiR-positive cells in tissues of DiR-C17.2-injected mice vs controls that did not receive DiR-C17.2 injections. DiR-C17.2-injected mice include C/C17.2 (medium gray, $N = 4$ per tissue except for spleen, $N = 0$ owing to processing error) and CML/C17.2 (light gray, $N = 22$ per tissue except for spleen, $N = 15$). Controls that did not receive DiR-C17.2 injections include C/0 and CML/0 and are collectively referred to as 'No DiR-C17.2' (dark gray; $N = 4$ for all tissues except spleen and tumor, $N = 2$). 'All Tissues' represents the average percentage of DiR-positive cells in all No DiR-C17.2 livers, spleens, marrow, tumors and kidneys ($0.35 \pm 0.22\%$, $N = 16$). Statistical significance ($p < 0.05$) is denoted with two asterisks when compared with All Tissues and by a single asterisk when compared with both the No DiR-C17.2 control for the same tissue and to the All Tissues control. Average percentage of DiR positive cells in tissues ± SD is as follows: liver (C/C17.2, $1.81 \pm 0.44\%$; CML/C17.2, $7.76 \pm 5.79\%$), marrow (C/C17.2, $1.50 \pm 0.66\%$; CML/C17.2, $2.13 \pm 1.37\%$), spleen (C/C17.2, $1.81 \pm 0.44\%$; CML/C17.2, $7.76 \pm 5.79\%$), tumor (CML/C17.2, $0.74 \pm 0.61\%$) and kidney (C/C17.2, $0.56 \pm 0.04\%$; CML/C17.2, $1.00 \pm 0.48\%$). Both the C/C17.2 and CML/C17.2 liver and marrow and the CML/C17.2 spleen and kidney demonstrated higher proportions of DiR-positive cells than both their matched tissue controls and the All Tissues control. Tumors showed a significantly higher proportion of DiR-positive cells as compared with the All Tissues control. There is no significant difference in the percentage of DiR-positive cells in the C/C17.2 vs CML/C17.2 livers, spleens, marrow and kidneys.

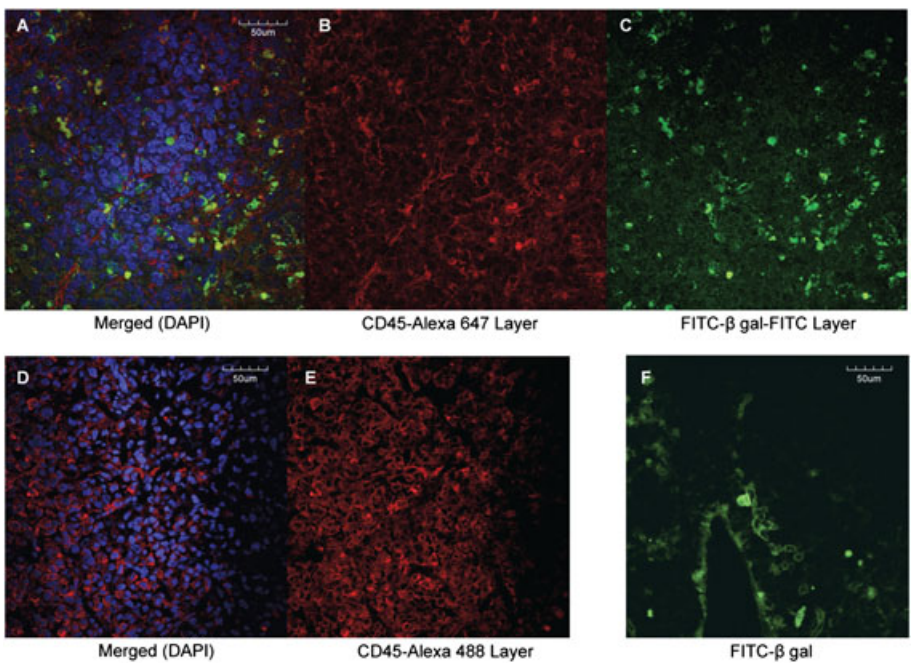

Figure 5. IF analysis of CML/C17.2 tumors using CD45 antibody conjugated to Alexa 647 or Alexa 488 (red) to evaluate for human tumor cell engraftment, FITC-β gal antibody (green) to evaluate for C17.2 cells, and DAPI (blue) as a nuclear marker. Displayed are the merged images (A, D), individual CD45 red layers (B, E) and individual FITC-β gal green layer (C). The last image (F) shows CML/C17.2 tumor stained with FITC-β gal antibody alone to eliminate the possible confounder of spectral bleed-through from other fluorophores. CML/C17.2 tumors demonstrate high numbers of red CD45-Alexa 647-positive human cells (A, B) and frequent clusters of green FITC-β-gal-positive cells (A, C, E) throughout the tumor. CD45-Alexa 488 staining of CML/C17.2 tumors (D, E) confirms that the majority of tumor cells express human CD45 (red).

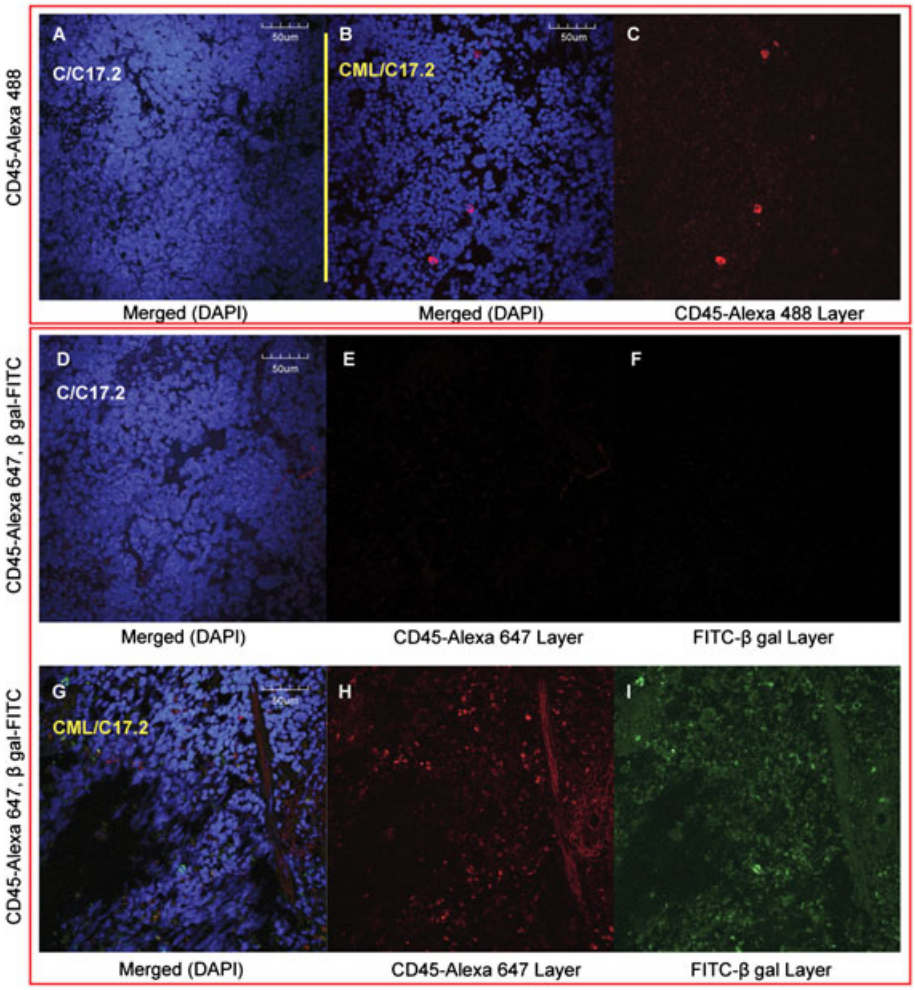

Figure 6. IF analysis of C/C17.2 (A, D–F) and CML/C17.2 (B, C, G–I) spleens using CD45-Alexa 488 (red; first row) or CD45-Alexa 647 (second and third rows) to evaluate for human tumor cell engraftment, FITC-β gal antibody (green; second and third rows) to evaluate for C17.2 cells, and DAPI (blue) as a nuclear marker. The merged images are in the first column and middle column for (B). The CD45 red layers (C, E, H) and the FITC-β gal green layers (F, I) are depicted separately. Rare red CD45-positive cells were detected in CML/C17.2 spleens (B, C) but none in C/C17.2 spleens (A, D, E). Rare green FITC-positive cells were seen in the CML/C17.2 spleens (I) and none in the C/C17.2 control spleens (F).

No CD45-positive cells were observed in control tissues (C/0 or C/C17.2, Figs 5–7).

Clusters of FITC-β gal-positive cells were scattered throughout the tumor parenchyma, often surrounding vessels, constituting $\leq$10% of total cells (30–100 cells) per high-powered field (Fig. 5). The other CML/C17.2 tissues demonstrated far fewer FITC-β gal-positive cells, with rare FITC-β gal-positive cells in spleens ($\leq$0.2% or 0–2 cells per high powered field; Fig. 6) and kidneys ($\leq$0.9% or 0–2 cells per high-powered field; Fig. 7). No FITC-β gal-positive cells were observed in tissues of mice that did not receive DiR-C17.2 cells (C/0 or CML/0; Figs 5–7).

In summary, CML tumors showed the highest levels of human engraftment by FACS (>67%) and IF (>83%) whereas CML spleens and kidneys demonstrated lower CD45+ engraftment by FACS (3.5 and 10.7%, respectively) and IF (<1% for both). The strongest DiR signal and largest number of DiR + cells were observed by imaging and FACS in the livers, spleens and marrow of both C/C17.2 and CML/C17.2 mice. By contrast, IF analysis revealed the highest concentration of β gal-positive cells to be within the tumors, with the numbers in CML spleens and CML kidneys to be low but proportional to the level of human cancer cell engraftment. No FITC-β gal-positive cells were detected in the tissues of mice that did not receive DiR-C17.2 cells and no CD45-positive cells were detected in the tissues of Control (untransplanted) mice.

3. DISCUSSION

The development of imaging modalities based on the targeting of malignant cells could dramatically improve cancer diagnosis and monitoring and present an opportunity to combine imaging with the directed delivery of treatment, termed theragnostics. A promising candidate for these purposes is the exploitation of NPC homing to tumors; NPC can be labeled with contrast agents for imaging and engineered to carry anti-tumor genes and therapies. Because cancers grown from malignant cells harvested from patients reflect the complexity that cancer exhibits clinically, we aimed to develop a model of NPC homing to patient-derived tumors.

The data presented demonstrate that CML tumors, which comprise primarily human cancer cells, retain intact C17.2 cells

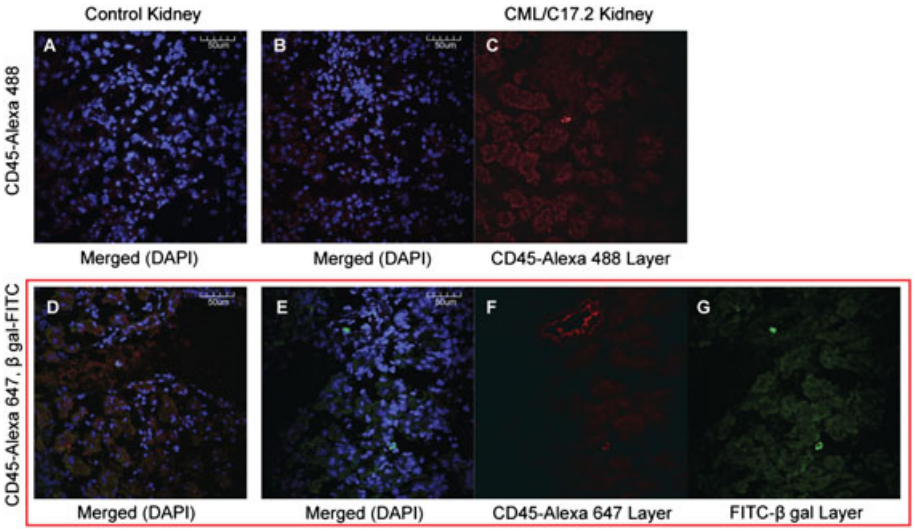

Figure 7. IF analysis of control kidneys (A, C/0; D, C/C17.2) and CML/C17.2 kidneys (B, C, E, F, G) using CD45-Alexa 488 (red; top row) or CD45-Alexa 647 (red; bottom row) to evaluate for human tumor cell engraftment, FITC-β gal antibody (green; D, E, G) to evaluate for C17.2 cells, and DAPI (blue) as a nuclear marker. Merged images are in the first and second columns, the CD45 red layers are in the third column and the FITC-β gal green layer is in the fourth column. Rare CD45-positive cells were seen in CML/C17.2 kidneys stained with CD45-Alexa 488 (C) and none in C/0 kidneys (A, D). Rare FITC-positive cells were seen in the CML/C17.2 kidneys (G) and none in the C/C17.2 control kidneys (D).

within the parenchyma at levels detectable by *ex vivo* optical imaging and confirmed by IF and FACS. CML spleens and kidneys, which contain much lower levels of cancer cell engraftment, retain proportionately fewer C17.2 cells. By contrast, C17.2 cells are not retained by tissues without cancer cell engraftment. Together these data suggest that C17.2 NPC home to highly engrafted patient-derived CML tumors and that this homing can be detected by *ex vivo* optical imaging. Perhaps more clinically significant, however, is the observation that C17.2 cells home at proportionately lower levels to tissues bearing low levels of malignant engraftment, in the absence of solid tumors. This finding suggests that C17.2 cells are capable of homing to micrometastatic disease. The detection of micrometastatic foci remains a challenge using conventional modalities such as CT, MRI and Positron Emission Tomography (PET). Thus, the propensity for C17.2 cells to home to patient-derived cancer cells could be used as a model to develop cellular homing technologies for the identification of metastatic disease as well as for the diagnosis of cancer, monitoring of treatment response, and the targeted delivery of treatment in patients.

Although prior studies have demonstrated NPC homing to cell line-derived solid tumors (2–4) and metastatic disease (18,21,36), to our knowledge, this is the first study demonstrating NPC homing to patient cancer cells. The niche requirements, growth characteristics and metastatic profile of patient-derived cancers closely mirror those of their cancer of origin; therefore a model of NPC homing to patient-derived cancers is more likely to reflect the complex interactions that govern cell migration (25,26,28). However, the inherent heterogeneity of patient-derived tumors can lead to increased variance in the data and may have decreased the statistical power to detect differences between the CML/C17.2 and C/C17.2 groups in the present study. For example, despite intrahepatic transplantations of equal numbers of CD34+/CD45+ cells from a single patient, performed by a single operator, there were wide variations in tumor number and gross tumor mass, which is typical of this murine xenograft model. It is possible that the concentration of NPC in target tissues is affected by the size and number of these tumors. Future studies using a higher *N* per experiment could focus on addressing these questions.

While DiR's robust signal and relatively good tissue penetration make it well-suited for tracking live cells in small animals over time, its durability results in the persistence of DiR in the membranes of dead cells and debris. Phagocytosis of this labeled debris by macrophages can make these cells appear DiR-positive. DiR can also be transferred directly to neighboring cells to such a significant degree, according to a recent study, that the authors recommend rigorous cross-validation through IF (37). Thus, the persistence of DiR signal in dead cells and the transfer of DiR from target cells to nontarget cells can result in DiR signal arising from sources other than the live C17.2 NPC originally labeled. These phenomena could help explain the high DiR signal detected by imaging and FACS in the spleens of control and CML mice despite the relative lack of FITC-β-gal-positive cells detected in the spleens by IF. The spleen, marrow, liver and lungs contain high concentrations of cells of the mononuclear phagocyte system (formerly 'the reticuloendothelial system') (38). As such, the high signal in these organs probably reflects the accumulation of phagocytic cells that have taken up DiR-labeled debris and the transfer of DiR to surrounding cells. To circumvent these issues, future studies could be carried out using C17.2 cells that stably express luciferase for bioluminescence imaging, where the photons are generated by a chemical reaction catalyzed by luciferase. Bioluminescence imaging tends to be more sensitive than fluorescence imaging, where the signal depends on the excitation of a fluorophore by light of one wavelength resulting in the emission of light of another wavelength, both of which are subject to attenuation and scatter. However, one disadvantage of bioluminescence imaging is that *ex vivo* imaging cannot be performed as reliably with this method since the luminescent signal peaks within minutes after intravenous or intraperitoneal administration of the luciferin substrate.

Another factor that probably contributed to the high signal in tissues such as the lungs, liver and spleen is cell filtration and sequestration. High DiR signal detected in the lungs immediately post-injection reflects trapping of DiR-positive cells in the pulmonary capillary bed. Variations on the method of delivery could reduce the number of cells in non-target tissues, including intra-arterial, intraosseous and intraperitoneal routes as well as percutaneous intratumoral injections. These methods of delivery of NPC would minimize cell trapping in the lungs and may minimize sequestration of cells by the liver, spleen and marrow. Intra-arterial, catheter-directed delivery would increase the concentration of cells in the vicinity of the highest tumor burden and could be used in combination with other catheter-directed treatments, suggesting a role for Interventional Radiology in this technology.

Future studies should concentrate on characterizing the biochemical processes by which C17.2 cells accumulate in tumors and in tissues with low levels of cancer cell engraftment, which may indicate homing to micrometastatic disease. Prior studies evaluating the factors directing C17.2 homing to cell line-derived tumors have identified roles for integrins (3), urokinase plasminogen activator (8), phosphoinositide 3-kinase signaling (9) and Vascular Endothelial Growth Factor (VEGF) (39). It is possible that homing to tissues engrafted with patient cancer cells occurs via many of the same mechanisms. Additionally, NPC homing to cancer cells in the absence of solid tumors may involve unique interactions with their niche, given the fact that these malignant cells live among normal cells and have not yet recruited their own blood supply.

Before NPC homing to tumors can be used as an imaging and therapeutic tool in humans, a more clinically applicable model must be developed. The first step would be to generate a human NPC line with tumor-homing properties comparable to C17.2 NPC. Although one strategy would be to harvest a patient's own NPC for this purpose, the development of a standard cell line would be less invasive and less costly and its safety, general immunocompatibility and homing properties could be characterized more thoroughly. Human NPC could be engineered to express antitumor agents in the form of genes, antibodies, enzymes, immune modulators and prodrugs (18–20,23). The results of the current study suggest that C17.2 NPC could be capable of delivering antitumor agents not only to solid tumors but also to micrometastatic disease, which could help to decrease cancer recurrence. Such targeted delivery could also permit high local concentrations of these therapies while minimizing side effects from high systemic doses. The next step would be to determine whether NPC homing may be imaged using a more clinically applicable modality. Although optical imaging is a safe and convenient modality for use in the development of an imaging model, it has limited applications in humans owing to poor tissue penetration beyond 2 cm. Future studies should determine whether C17.2 homing to patient-derived tumors is detectable by modalities such as nuclear imaging, ultrasound or MRI, as has been shown with cell line-derived tumors (10,11).

4. CONCLUSIONS

In conclusion, the potential to target cancer cells through NPC homing holds promise as a diagnostic and therapeutic tool for reaching sites of malignancy that are not yet visible radiographically and may be recalcitrant to current therapeutic regimens. This animal model of cellular homing to patient-derived tumors could help pave the way toward the successful development of these cell-based theragnostic strategies for cancer management.

5. EXPERIMENTAL

Please refer to Table 1 for a list of common abbreviations, including those used to denote each experimental group, and to Table 2 for a summary of the overall experimental design and *N* per group.

5.1. Murine model of human CML

The murine CML xenograft model has been described previously in detail (28,35,40). Briefly, neonatal rag2 γ chain IL-2$^{-/-}$ mice were transplanted intrahepatically with CD34+/CD45+ blast crisis CML cells (10^5–10^6 cells) derived from three different patients (the same patient sample was used for all transplanted mice within each of the three experiments). CML blood and marrow samples were donated by patients from University of California, San Diego (UCSD), Stanford University and MD Anderson Cancer Center according to Institutional Review Board (IRB) approved protocols. At 8–10 weeks post-transplantation, most animals developed solid vascular sarcomas throughout the body, occurring most frequently in the abdomen but also in the thorax, extremities and cervical region. Transplanted mice with palpable tumors were selected for the experiments. In order to reduce background fluorescence from abdominal contents, animals undergoing imaging were fed an alfalfa-free diet (no. 1813058 Purified Pico Rodent Irradiated Diet, Test-Diet, Newco Distributors). Animal health was monitored weekly then more frequently as tumors progressed. Mice weighed an average of 25 g. Gross tumor weight ranged from 3 to 8 g. The number of tumors per CML mouse ranged from 1 to 7 and averaged 2.4 tumors per CML mouse. All animal use protocols were pre-approved by the UCSD Institutional Animal Care and Use Committee.

5.2. C17.2 Labeling with DiR

As previously described (41), C17.2 NPC were derived from neonatal murine cerebellum and transduced via the MMLV retroviral vector with *vmyc* to enhance immortality and *lacZ* to permit stable expression of β-galactosidase. C17.2 NPC were grown and maintained in culture in Dulbecco's modified Eagle's medium (Gibco) supplemented with 10% fetal bovine serum (FBS; Gibco), 5% horse serum (Gibco), 1% L-glutamine (2 mM; Gibco) and 1% penicillin–streptomycin (Gibco), according to

Table 2. Experimental design

	All groups	C/0	C/C17.2	CML/0	CML/C17.2
Total *N*[a]	39	3	8	2	26
N FACS[b]	30	2	4[d]	2	22
N IF[c]	5	1	2	0	2

[a]*N* over three experiments, all evaluated by fluorescence optical imaging.
[b]*N* analyzed by FACS.
[c]*N* analyzed by IF.
[d]Data for the spleens of these mice are not included owing to processing error.

previously described methods (41), in 100 mm cell culture dishes and to approximately 70% confluence. Immediately prior to injection, adherent C17.2 cells were stained with the lipophilic near-infrared fluorescent dye DiR (1,1′-dioctadecyl-3,3,3′,3′-tetramethylindotricarbocyanine iodide, excitation 750, emission 780; Invitrogen), 9 μg/ml in phosphate buffered saline (PBS) for 15 min at 37 °C then 15 min at 4 °C. After gentle trypsinization, the stained cells were washed then filtered through a cell-strainer cap to remove cell aggregates and debris and the viable cells quantified on a hemocytometer using trypan blue and diluted with PBS to a final concentration of 0.5–1 $\times$ 10^6 cells per 100 μl.

Prior to *in vivo* experiments, *in vitro* optimization of this protocol was performed in a 96-well plate, which revealed that the lower limits of detection of C17.2 cells stained with DiR according to the methods described is 1.25 $\times$ 10^5 cells with a 10 s exposure and 2.5 $\times$ 10^5 cells with a 5 s exposure.

5.3. Animal administration of DiR-labeled C17.2 cells

Intravenous (i.v.) injections of DiR-labeled C17.2 cells (DiR-C17.2) were performed via the tail vein of CML mice (CML/C17.2, $N = 28$) or controls (untransplanted mice, C/C17.2, $N = 8$). Daily injections of 1 $\times$ 10^6 cells in 100–200 μl PBS were administered for 1–4 days (except for the last dose, which was 5 $\times$ 10^5 cells in the same volume), for up to five doses, with a total dose of up to 4.5 $\times$ 10^6 cells. This schedule was adopted to permit the administration of a larger total number of cells while avoiding the significantly higher immediate post-injection mortality observed after doses greater than 1.5 $\times$ 10^6 cells. Despite cell filtration, a majority of the mice given i.v. injections of more than 1.5 $\times$ 10^6 cells in a single dose developed post-injection acute dyspnea, leading to sudden death. On necropsy, these mice demonstrated numerous bilateral small wedge-shaped pulmonary infarcts, presumably due to cell trapping in the distal pulmonary vasculature.

Both untransplanted mice (C/0, $N = 3$) and CML transplanted mice (CML/0, $N = 3$) that did not receive injections of DiR-C17.2 cells served as additional controls (Table 2).

5.4. Optical fluorescence imaging

Anesthetized mice were imaged optically using the Xenogen IVIS® 200 Series imaging system (Caliper Life Sciences, Hopkinton, MA, USA) within the first 10–100 min post-injection to exclude large extravasations and to confirm adequate injection; thus these images were not included in the data analysis and are not reflected in Fig. 2. Daily imaging was performed for up to 4 days (at 24, 48, 72 and 96 h) post-initial injection, with imaging occurring approximately 3 h after each subsequent injection to permit cells to clear the lungs and exit the blood pool. Imaging across time points was performed to assess the biodistribution of the fluorescent signal over time and to insure detection of any potential peaks or fluctuations in homing (due to the possibility of cells exiting the target tissue or cell death and phagocytosis) and not expressly to characterize the time course of homing. As the pattern of fluorescent signal remained stable from 24 through 96 h and no significant differences were subsequently demonstrated in either the fluorescence imaging or FACS, the data from the time points were combined for analysis.

Mice were imaged supine and the few mice in which tumors grew dorsally were also imaged prone. A C/0 or CML/0 mouse was included in each imaging set as a negative control, as they did not receive DiR-C17.2 cell injections; they displayed the same low level of background fluorescence and were thus used interchangeably. Fluorescence ICG emission and excitation filters were used with 5–15 s exposure times, using fields of view to accommodate three, four or five mice. Larger fields of view permitted direct comparison among a greater number of animals at the expense of lower detected photons due to scatter. Because of this and inherent differences in the intensity of fluorescence among mice and tissues and owing to necessary differences in imaging parameters for optimization, displayed fluorescence levels were normalized to the control within each set and displayed with their own scale bars.

Directly after each of the four imaging time points (24, 48, 72 and 96 h), a subset of mice was sacrificed humanely by carbon dioxide asphyxiation (Table 2; N per subset = 4–6 CML/C17.2, 2–4 C/C17.2, 1 C/0, 1 CML/0). Post-mortem, the viscera were exposed and imaged *in situ* then removed and imaged *ex vivo* in order to reveal low levels of fluorescence that were attenuated by overlying structures or was below the level of detection when imaged with strongly fluorescent organs. Images were analyzed using Living Image® Software and DiR signal was quantified within designated regions of interest as total photons per second per square centimeter per steradian (p/s/cm^2/sr). Control tissues which had not received DIR-C17.2 NPC were also measured to determine background levels of fluorescence, but only one or two control samples per tissue group emitted measurable signal. The average radiance of all control tissues with measurable signal was 7.60 $\times$ 10^6 $\pm$ 1.27 $\times$ 10^6; this value probably overestimates the average background radiance since it does not include those that were below the level of detection. Positive fluorescence was thus defined as greater than or equal to one standard deviation above the average measurable background levels in control tissues, or $\geq$9 $\times$ 10^6 p/s/cm^2/sr.

5.5. Tissue processing for FACS and IF

The liver, spleen, bone marrow, kidneys, and tumors from 24, 48 and 96 h time points were harvested and homogenized, then analyzed by FACS either immediately or the homogenized tissues frozen in bovine serum albumin (Sigma) and FACS performed at a later date ($N = 33$, Table 2). The tissues from the 24, 48 and 96-h time points were dedicated for FACS experiments. The heart was not included in the FACS analysis because of technical limitations on the number of samples which could be analyzed in each FACS experiment and because the heart of the murine CML xenograft is not routinely analyzed in our laboratory, so there is no internal reference data for expected levels of engraftment. The harvested tissues from the 72 h time point were flash frozen for IF ($N = 5$). Tissues from the 72 h time point, in which mice received the second highest total dose (4 $\times$ 10^6 cells), were dedicated for IF analysis in order to minimize variance by comparing tissues from within a single time point. Apart from IF analysis of the tumors, which represent a tissue with low fluorescent signal but high engraftment, the spleens were selected for IF because they represent a tissue with high fluorescent signal but low engraftment whereas the kidneys were selected because they represent a tissue with low fluorescent signal and low engraftment. The bone marrow, liver and heart were also collected and flash frozen for IF analysis as part of future experiments.

5.6. FACS analysis

For FACS analysis, homogenized tissues were washed then blocked in Mouse Fcγ receptor III/II (1:25, BD Biosciences) and

Anti-Human FcR blocking reagent (1:25, Miltenyi Biotec) in HBSS (Mediatech) with 2% fetal bovine serum (Gemini Bio-products). Blocked cells were then incubated with CD45-APC antibody (1:50, Invitrogen) or CD45-Alexa 405 antibody (1:50, Invitrogen) in HBSS with 2% FBS to detect human engraftment then eluted in propidium iodide (PI, 1:2000, Fisher Scientific) to exclude dead cells. The near-infrared fluorescent signal emitted by the DiR-positive cells was detected directly by FACS. At least 2×10^5 cells were analyzed per sample. Appropriate standard controls, fluorescence minus one controls and compensation controls were included in each experiment. FACS analysis was performed on a FACS Aria I (BD Biosciences) and the data analyzed using FloJo Software, Version 8.8.7.

5.7. IF

For IF analysis, harvested tissues were embedded in Tissue-Tek O.C.T. compound (VWR International), flash frozen, then stored at -80 °C prior to sectioning (8–10 μm thickness). C17.2 cells were detected using FITC-conjugated β-galactosidase antibody (FITC-β gal; Abcam) and human CML cells were detected using CD45 antibody conjugated to Alexa 488 (Invitrogen) or Alexa 647 (Biolegend). Alexa 488 provides a more robust signal than does Alexa 647 but could not be used concurrently with the β-galactosidase-FITC antibody, as both are excited by the 488 laser. Nevertheless, the use of these two different fluorophores conjugated to CD45 antibody permitted discrimination of true fluorescence from potential autofluorescence or spectral bleed-through. However, for consistency and simplicity, all CD45 labeling is depicted here in red, although Alexa-488 is excited by the Argon 488 nm (green) laser and Alexa 647 by the HeNe 633 nm (red) laser.

Sections were first fixed and permeabilized in cold acetone for 5–10 min, washed in PBS, then blocked for 2 h with rat anti-mouse FcR (1:50) in Dulbecco's phosphate-buffered saline (DPBS)–5% bovine serum albumin (BSA)/5% FBS. Sections were then incubated for 1 h in DPBS–5%BSA/5%FBS in either CD45-Alexa 488 (1:50) alone or CD45-Alexa 647 (1:50) and FITC β-galactosidase antibody (1:200). After incubation, the sections were washed with cold PBS then coverslipped with Vectashield Hard Set mounting medium with 4′,6-Diamidino-2-Phenylindole, Dihydrochloride (DAPI) (Vector Laboratories) to counterstain the nuclei. Immunofluorescence was evaluated on an Olympus confocal microscope at 40× magnification then images viewed and processed using Olympus FluoView Software, version 2.0b.

5.8. Statistical analysis

Data is reported as the mean ± standard deviation (SD). Statistics were performed using a two-tailed Student's *t*-test with a *p*-value of 0.05. Statistical significance (<0.05) is denoted with asterisks in Figs 2–4, as described in the figure legends. Experimental groups were compared with controls within their group ($N = 1$–4 samples) and also with 'All Tissues' controls ($N = 10$–19), which represent an average of all of the negative control tissues for that experimental condition (refer to figure legends for Figs 2–4 for details).

Acknowledgments

Support was given by ICMIC P50 CA128346. Salary support for Isabel G. Newton was provided by NIH grant T32EB005970. We are grateful to all members of the Jamieson Laboratory, who each have contributed to the collection of data, and to Jonathan Lee for his skilled assistance in the preparation of the figures.

REFERENCES

1. Shackleton M, Quintana E, Fearon ER, Morrison SJ. Heterogeneity in cancer: cancer stem cells versus clonal evolution. Cell 2009; 138(5): 822–829.
2. Aboody KS, Brown A, Rainov NG, Bower KA, Liu S, Yang W, Small JE, Herrlinger U, Ourednik V, Black PM, Breakefield XO, Snyder EY. Neural stem cells display extensive tropism for pathology in adult brain: evidence from intracranial gliomas. Proc Natl Acad Sci USA 2000; 97(23): 12846–12851.
3. Allport JR, Shinde Patil VR, Weissleder R. Murine neuronal progenitor cells are preferentially recruited to tumor vasculature via alpha4-integrin and SDF-1alpha-dependent mechanisms. Cancer Biol Ther 2004; 3(9): 838–844.
4. Brown AB, Yang W, Schmidt NO, Carroll R, Leishear KK, Rainov NG, Black PM, Breakefield XO, Aboody KS. Intravascular delivery of neural stem cell lines to target intracranial and extracranial tumors of neural and non-neural origin. Hum Gene Ther 2003; 14(18): 1777–1785.
5. Reagan MR, Kaplan DL. Concise review: mesenchymal stem cell tumor-homing: detection methods in disease model systems. Stem Cells 2011; 29(6): 920–927.
6. Doucette T, Rao G, Yang Y, Gumin J, Shinojima N, Bekele BN, Qiao W, Zhang W, Lang FF. Mesenchymal stem cells display tumor-specific tropism in an RCAS/Ntv – a glioma model. Neoplasia 2011; 13(8): 716–725.
7. Gazeau F, Wilhelm C. Magnetic labeling, imaging and manipulation of endothelial progenitor cells using iron oxide nanoparticles. Future Med Chem 2010; 2(3): 397–408.
8. Gutova M, Najbauer J, Frank RT, Kendall SE, Gevorgyan A, Metz MZ, Guevorkian M, Edmiston M, Zhao D, Glackin CA, Kim SU, Aboody KS. Urokinase plasminogen activator and urokinase plasminogen activator receptor mediate human stem cell tropism to malignant solid tumors. Stem Cells 2008; 26(6): 1406–1413.nn.
9. Kendall SE, Najbauer J, Johnston HF, Metz MZ, Li S, Bowers M, Garcia E, Kim SU, Barish ME, Aboody KS, Glackin CA. Neural stem cell targeting of glioma is dependent on phosphoinositide 3-kinase signaling. Stem Cells 2008; 26(6): 1575–1586.
10. Thu MS, Najbauer J, Kendall SE, Harutyunyan I, Sangalang N, Gutova M, Metz MZ, Garcia E, Frank RT, Kim SU, Moats RA, Aboody KS. Iron labeling and pre-clinical MRI visualization of therapeutic human neural stem cells in a murine glioma model. PLoS One 2009; 4(9): e7218.
11. Waerzeggers Y, Klein M, Miletic H, Himmelreich U, Li H, Monfared P, Herrlinger U, Hoehn M, Coenen HH, Weller M, Winkeler A, Jacobs AH. Multimodal imaging of neural progenitor cell fate in rodents. Mol Imag 2008; 7(2): 77–91.
12. Bulte JW. In vivo MRI cell tracking: clinical studies. AJR Am J Roentgenol 2009; 193(2): 314–325.
13. Lin D, Najbauer J, Salvaterra PM, Mamelak AN, Barish ME, Garcia E, Metz MZ, Kendall SE, Bowers M, Kateb B, Kim SU, Johnson M, Aboody KS. Novel method for visualizing and modeling the spatial distribution of neural stem cells within intracranial glioma. Neuroimage 2007; 37 Suppl 1: S18–26.
14. Walczak P, Kedziorek DA, Gilad AA, Barnett BP, Bulte JW. Applicability and limitations of MR tracking of neural stem cells with asymmetric cell division and rapid turnover: the case of the shiverer dysmyelinated mouse brain. Magn Reson Med 2007; 58(2): 261–269.
15. Aboody KS, Najbauer J, Danks MK. Stem and progenitor cell-mediated tumor selective gene therapy. Gene Ther 2008; 15(10): 739–752.
16. Allport JR, Weissleder R. In vivo imaging of gene and cell therapies. Exp Hematol 2001; 29(11): 1237–1246.
17. Cihova M, Altanerova V, Altaner C. Stem cell based cancer gene therapy. Mol Pharm 2011; 8(5): 1480–1487.
18. Dickson PV, Hamner JB, Burger RA, Garcia E, Ouma AA, Kim SU, Ng CY, Gray JT, Aboody KS, Danks MK, Davidoff AM. Intravascular administration of tumor tropic neural progenitor cells permits targeted delivery of interferon-beta and restricts tumor growth in a murine model of disseminated neuroblastoma. J Pediat Surg 2007; 42(1): 48–53.
19. Danks MK, Yoon KJ, Bush RA, Remack JS, Wierdl M, Tsurkan L, Kim SU, Garcia E, Metz MZ, Najbauer J, Potter PM, Aboody KS. Tumor-targeted

enzyme/prodrug therapy mediates long-term disease-free survival of mice bearing disseminated neuroblastoma. Cancer Res 2007; 67(1): 22–25.
20. Gutova M, Najbauer J, Chen MY, Potter PM, Kim SU, Aboody KS. Therapeutic targeting of melanoma cells using neural stem cells expressing carboxylesterase, a CPT-11 activating enzyme. Current Stem Cell Res Ther 2010; 5(3): 273–276.
21. Seol HJ, Jin J, Seong DH, Joo KM, Kang W, Yang H, Kim J, Shin CS, Kim Y, Kim KH, Kong DS, Lee JI, Aboody KS, Lee HJ, Kim SU, Nam DH. Genetically engineered human neural stem cells with rabbit carboxyl esterase can target brain metastasis from breast cancer. Cancer Lett 2011; 311(2): 152–159.
22. Serakinci N, Christensen R, Fahrioglu U, Sorensen FB, Dagnaes-Hansen F, Hajek M, Jensen TH, Kolvraa S, Keith NW. Mesenchymal stem cells as therapeutic delivery vehicles targeting tumor stroma. Cancer Biother Radiopharm 2011; 26(6): 767–773.
23. Frank RT, Najbauer J, Aboody KS. Concise review: stem cells as an emerging platform for antibody therapy of cancer. Stem Cells 2010; 28(11): 2084–2087.
24. Bianchi G, Borgonovo G, Pistoia V, Raffaghello L. Immunosuppressive cells and tumour microenvironment: focus on mesenchymal stem cells and myeloid derived suppressor cells. Histol Histopathol 2011; 26(7): 941–951.
25. Bankert RB, Balu-Iyer SV, Odunsi K, Shultz LD, Kelleher RJ, Jr, Barnas JL, Simpson-Abelson M, Parsons R, Yokota SJ. Humanized mouse model of ovarian cancer recapitulates patient solid tumor progression, ascites formation, and metastasis. PLoS One 2011; 6(9): e24420.
26. Wege AK, Ernst W, Eckl J, Frankenberger B, Vollmann-Zwerenz A, Mannel DN, Ortmann O, Kroemer A, Brockhoff G. Humanized tumor mice – a new model to study and manipulate the immune response in advanced cancer therapy. Int J Cancer 2011; 129(9): 2194–2206.
27. Shinde Patil VR, Friedrich EB, Wolley AE, Gerszten RE, Allport JR, Weissleder R. Bone marrow-derived lin(−)c-kit(+)Sca-1+ stem cells do not contribute to vasculogenesis in Lewis lung carcinoma. Neoplasia 2005; 7(3): 234–240.
28. Jamieson CH, Ailles LE, Dylla SJ, Muijtjens M, Jones C, Zehnder JL, Gotlib J, Li K, Manz MG, Keating A, Sawyers CL, Weissman IL. Granulocyte-macrophage progenitors as candidate leukemic stem cells in blast-crisis CML. New Engl J Med 2004; 351(7): 657–667.
29. Mishra A, Shiozawa Y, Pienta KJ, Taichman RS. Homing of cancer cells to the bone. Cancer Microenviron 2011; 4(3): 221–235.
30. Daley GQ, Van Etten RA, Baltimore D. Induction of chronic myelogenous leukemia in mice by the P210bcr/abl gene of the Philadelphia chromosome. Science 1990; 247(4944): 824–830.
31. Druker BJ, Guilhot F, O'Brien SG, Gathmann I, Kantarjian H, Gattermann N, Deininger MW, Silver RT, Goldman JM, Stone RM, Cervantes F, Hochhaus A, Powell BL, Gabrilove JL, Rousselot P, Reiffers J, Cornelissen JJ, Hughes T, Agis H, Fischer T, Verhoef G, Shepherd J, Saglio G, Gratwohl A, Nielsen JL, Radich JP, Simonsson B, Taylor K, Baccarani M, So C, Letvak L, Larson RA. Five-year follow-up of patients receiving imatinib for chronic myeloid leukemia. New Engl J Med 2006; 355(23): 2408–2417.
32. Fialkow PJ, Jacobson RJ, Papayannopoulou T. Chronic myelocytic leukemia: clonal origin in a stem cell common to the granulocyte, erythrocyte, platelet and monocyte/macrophage. Am J Med 1977; 63(1): 125–130.
33. Radich JP, Dai H, Mao M, Oehler V, Schelter J, Druker B, Sawyers C, Shah N, Stock W, Willman CL, Friend S, Linsley PS. Gene expression changes associated with progression and response in chronic myeloid leukemia. Proc Natl Acad Sci USA 2006; 103(8): 2794–2799.
34. Huang X, Cortes J, Kantarjian H. Estimations of the increasing prevalence and plateau prevalence of chronic myeloid leukemia in the era of tyrosine kinase inhibitor therapy. Cancer 2012; 118(12): 3123–3127.
35. Abrahamsson AE, Geron I, Gotlib J, Dao KH, Barroga CF, Newton IG, Giles FJ, Durocher J, Creusot RS, Karimi M, Jones C, Zehnder JL, Keating A, Negrin RS, Weissman IL, Jamieson CH. Glycogen synthase kinase 3beta missplicing contributes to leukemia stem cell generation. Proc Natl Acad Sci USA 2009; 106(10): 3925–3929.
36. Aboody KS, Najbauer J, Schmidt NO, Yang W, Wu JK, Zhuge Y, Przylecki W, Carroll R, Black PM, Perides G. Targeting of melanoma brain metastases using engineered neural stem/progenitor cells. Neuro Oncol 2006; 8(2): 119–126.
37. Lassailly F, Griessinger E, Bonnet D. 'Microenvironmental contaminations' induced by fluorescent lipophilic dyes used for noninvasive in vitro and in vivo cell tracking. Blood 2010; 115(26): 5347–5354.
38. van Furth R, Cohn ZA, Hirsch JG, Humphrey JH, Spector WG, Langevoort HL. The mononuclear phagocyte system: a new classification of macrophages, monocytes, and their precursor cells. Bull WHO 1972; 46(6): 845–852.
39. Schmidt NO, Koeder D, Messing M, Mueller FJ, Aboody KS, Kim SU, Black PM, Carroll RS, Westphal M, Lamszus K. Vascular endothelial growth factor-stimulated cerebral microvascular endothelial cells mediate the recruitment of neural stem cells to the neurovascular niche. Brain Res 2009; 1268: 24–37.
40. Zhao C, Chen A, Jamieson CH, Fereshteh M, Abrahamsson A, Blum J, Kwon HY, Kim J, Chute JP, Rizzieri D, Munchhof M, VanArsdale T, Beachy PA, Reya T. Hedgehog signalling is essential for maintenance of cancer stem cells in myeloid leukaemia. Nature 2009; 458(7239): 776–779.
41. Snyder EY, Deitcher DL, Walsh C, Arnold-Aldea S, Hartwieg EA, Cepko CL. Multipotent neural cell lines can engraft and participate in development of mouse cerebellum. Cell 1992; 68(1): 33–51.